CCFE
CULHAM CENTRE FOR FUSION ENERGY

UK Atomic Energy Authority

UKAEA-CCFE-PR(24)260

J.C Haley, H. Dawson, S. Jones, S. Mehraban, N. Lavery, J. Cullen, M. Carter, M. Moody, D. Bowden

Short Communication: Complete dissolution of MX-phase nanoprecipitates during irradiation by heavy-ions

Short Communication: Complete dissolution of MX-phase nanoprecipitates during irradiation by heavy-ions

J.C Haley, H. Dawson, S. Jones, S. Mehraban, N. Lavery, J. Cullen, M. Carter, M. Moody, D. Bowden

This is a preprint of a paper submitted for publication in Journal of Nuclear Materials

Short Communication: Complete dissolution of MX-phase nanoprecipitates in fusion steels during irradiation by heavy-ions

Jack Haley[ac], Stephen Jones[b], Shahin Mehraban[b], Nicholas Lavery[b], Jonathan Cullen[b], Megan Carter[c], Michael Moody[c], Huw Dawson[ad], David Bowden[a]

[a] *UKAEA, Culham Campus, Abingdon, Oxfordshire OX14 3DB, UK*

[b] *Future Manufacturing Research Institute, College of Engineering, Swansea University, Bay Campus, Fabian Way, Swansea, SA1 8EN, UK*

[c] *Department of Materials, University of Oxford, Parks Road, Oxford OX1 3PH, UK*

[d] *Frazer-Nash Consultancy Limited, Hill Park Court, Springfield Drive, Leatherhead, Surrey, KT22 7NL*

Accepted submission April 2024 *Corresponding author email address: jack.haley@ukaea.uk*

Abstract

New RAFM steels, with intragranular VN precipitates for enhanced creep strength, were irradiated with 2MeV Fe+ ions at 600°C to explore MX-type precipitate response to extreme end-of-life conditions in breeder blanket components. Utilizing TEM, Analytical-STEM, and APT, the steels were characterized in the unirradiated and irradiated states. Unirradiated grains contained needle-like VN precipitates (~$1x10^{22}/m^2$). However, throughout the 40-100 dpa irradiation damage layer, VN precipitates were completely annihilated. APT confirmed no fine-scale VN clustering, indicating re-solution with the matrix, suggesting instability. Further investigations via reactor irradiations are crucial to assess this instability under breeder blanket conditions.

Reduced Activation Ferritic Martensitic (RAFM) steels have been developed for use in nuclear fusion reactors, such as Eurofer-97 and F82H [1]. Research into new RAFM variants has continued in attempt to extend the operational temperature range of such steels (for example, [2,3]), which are typically limited to ~350 to 550°C [4]. Efforts to increase the maximum allowable temperature of RAFM steels are often focussed on increasing the creep rupture strength of a steel, but a critical challenge is to do so while retaining adequate fracture toughness. A fine grain-size microstructure is not only good for fracture toughness, but also appears to be effective at delaying the effects of low temperature hardening embrittlement (LTHE) <350°C [5]. Concurrently, it is well-known that larger grain microstructures are important for reducing the creep-strain rate at high temperatures [6], but this would likely lead to accelerated losses in ductility due to hardening embrittlement [5]. Another strategy to extending the creep lifetime of an alloy is to refine the precipitates in the microstructure [6]. This would potentially allow for a finer grain structure (for delaying LTHE and maintaining adequate toughness), while also increasing the creep strength.

During creep, martensitic steels gradually soften due to laths, packets and blocks coarsening, with the microstructure gradually evolving towards equiaxed ferrite. This recovery of martensite during creep is the primary cause of loss of strength and rupture. Two types of precipitate are most typically utilised in martensitic steels, $M_{23}C_6$ and MX. The $M_{23}C_6$ precipitates (M being mostly Cr) are large (up to 100s of nm) and primarily located on lath, packet, block and prior-austenite grain (PAG) boundaries. MX-type precipitates (in RAFM steels, M being Ta, V or Ti, and X being C or N, or both) are smaller (10s of nm), and located inside grains or on boundaries. Their higher thermal stability relative to $M_{23}C_6$ means they have the potential to pin grain boundaries for longer, delaying the recovery of martensite, while intragranular precipitates are effective barriers to dislocations. Thus, new RAFM alloy compositions and thermomechanical treatments are being developed to target microstructures with a higher density of fine MX-type nanoprecipitates relative to conventional RAFM steels, such as Eurofer-97 and F82H [2,9].

A critical question arises: what is the susceptibility of these fine MX precipitates to dissolution during irradiation? Previous authors have sought to address this question. Tanigawa et al. [10] found the MX phase (TaC) in steels JLF1 and ORNL 9Cr2WVTa disappeared after irradiation (5 dpa neutrons, 300°C), according to the loss of MX-peaks in XRD spectra relative to measurements on the unirradiated alloys. Later ion-irradiations by Tanigawa et al. [11] of a model Fe-Ta-C alloy showed, via TEM, the re-solution of the TaC precipitates after irradiation (up to 20 dpa single/dual-ions, 500°C). Conversely, Tan et al. later found MX to be comparatively stable during irradiation. Tan et al. [12] self-ion irradiated model alloys containing either TaC, TaN or VN, up to 49 dpa at 500°C, and used TEM to show only slight dissolution. A slight increase in density and reduction in size was noted

Table 1: Composition in wt% of Alloys 1 and 2, and similar RAFM alloys. Superscript denotes the at% composition.

Alloy	Cr	W	Mn	V	Ta	C	N	Si	P (x10^{-3})	S (x10^{-3})
Alloy-1	8.7 $^{9.0}$	2.1 $^{0.6}$	0.26 $^{0.25}$	0.30 $^{0.3}$	0.04 $^{0.01}$	0.06 $^{0.3}$	0.036 $^{0.14}$	0.15 $^{0.3}$	<0.7	4.0
Alloy-2	8.8 $^{9.2}$	1.2 $^{0.35}$	0.25 $^{0.25}$	0.21 $^{0.2}$	0.08 $^{0.02}$	0.08 $^{0.36}$	0.028 $^{0.11}$	0.11 $^{0.2}$	<0.7	3.0
Eurofer-97 ^{3i}	8.8	1.1	0.54	0.20	0.12	0.10	0.037	0.02	0.9	1.6
ORNL-9Cr-2WVTa ^{3791}	8.7	2.1	0.43	0.23	0.08	0.10	0.022	0.23	15.0	5.0

Compositions of Eurofer97 and ORNL-9Cr-2WVTa taken from references [7,8] *respectively, and the batch identifier is indicated by superscript.*

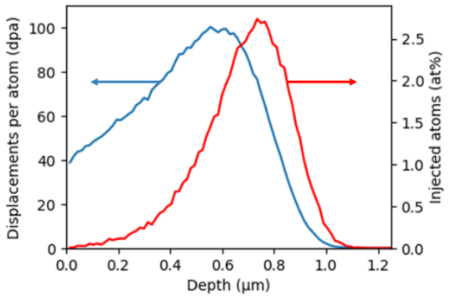

Figure 1: SRIM calculated damage-depth profile of 2MeV Fe+ implanted into Fe. Also shown is the injected Fe+ profile.

as a function of dose, with the dissolution more pronounced beyond the Bragg peak. Kano et al. [13] also showed in F82H (BA12 variant) that there was only a slight reduction in the size of Ta/C-rich MX precipitates after self-ion irradiation to 50 dpa at 400ºC. Later, Tan et al. [14] showed the orientation of VN needles/platelets with respect to the ion-beam affects the dissolution. Needles oriented in the direction of the ion-beam were susceptible to growth in length and eventual splitting, leading to an increase in their number density, but with a refined size. Those oriented normal to the beam underwent splitting, but also complete dissolution of the smaller precipitates leading to a reduction in number density. Neutron irradiation by Tan et al. [15] up to 7.4 dpa at 490ºC of CNA1 steel contained MX (V/Ta, C/N) with only a slight (~5%) reduction in size. In this work, the intragranular MX-type (VN) nanoprecipitates in 9Cr-1.2-2WVTa RAFM steels are investigated, and what happens to them after high-dose irradiation is analysed and compared with earlier works.

The steels used were produced by UKAEA in collaboration with Swansea University. The alloy compositions are listed in Table 1. Also listed in Table 1 for comparison are compositions of Eurofer-97 and ORNL 9Cr2WVTa alloy.

The steels underwent a series of thermomechanical heat treatments designed to favour the formation of a high density of VN precipitates, with the intention of improving the creep strength. The alloys underwent hot-rolling, with a reduction of ~50%, and were then held at 900ºC, which is above the formation temperature for $Cr_{23}C_6$. This step was performed to allow a longer time for VN to nucleate and coarsen before quenching and tempering of the steel. The heat-treatments and backscatter SEM micrographs of the steels are depicted in the Supplementary Material.

Irradiation was conducted at the University of Surrey Ion Beam Centre, using 2 MeV Fe+ ions at a temperature of 600ºC. The samples were irradiated to a total fluence of $9x10^{16}$ ions/cm^2 over 7hrs 40 mins, which achieved a displacements per atom (dpa) dose ranging from 40 dpa at the surface to 100 dpa at the Bragg peak, with a high dose rate of $1\text{-}3x10^{-3}$ dpa/s. Figure 1 shows the dpa profile, generated by SRIM software [16], using the quick Kinchen-Pease method, a displacement energy set to 40eV, and lattice binding energy set to zero [17,18].

Samples for TEM were produced via the focussed ion beam (FIB) lift-out method [19]. FIB was conducted at the Materials Research Facility (MRF) at UKAEA using a FEI Helios Nanolab 600i, with a Ga beam energy set to 30kV for thinning the foil and 2kV for final cleaning. TEM was conducted at the David Cockayne Centre for Electron Microscopy (DCCEM), University of Oxford, using a Jeol 2100L with LaB_6 source operating at 200 kV. Electron Energy Loss Spectroscopy (EELS) was also performed at DCCEM using a Jeol ARM cold-FEG STEM operating at 200 kV. A Gatan Imaging Filter was used, with convergence angle of 31.5 mrad, and collection half-angles of 41 mrad.

Atom Probe Tomography (APT) was conducted on needles lifted from the irradiated and unirradiated parts of the sample at DCCEM, with the APT carried out on a Cameca LEAP 5000XR atom probe at the University of Oxford. Standard atom probe FIB lift-out procedures were adopted [20], with a 2kV cleaning polish applied to the final

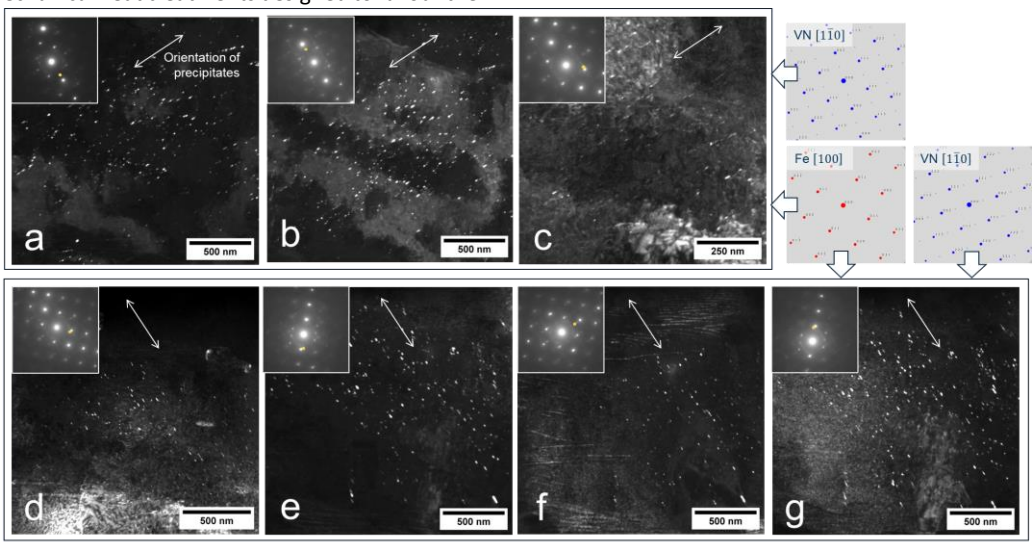

Figure 2: Dark-field TEM micrographs showing MX nanoprecipitates in Alloy 1 in the unirradiated condition. Each micrograph, (a)-(g) shows the same area, imaged with a different reflection and each with parallel beam illumination to avoid spot overlap. White arrows indicate the direction in which the precipitates are aligned. The diffraction pattern for each dark-field condition is shown, and the position of the objective aperture is shown by a yellow circle at the correct scale. Computer generated patterns of Fe BCC and VN FCC phases are also shown [21].

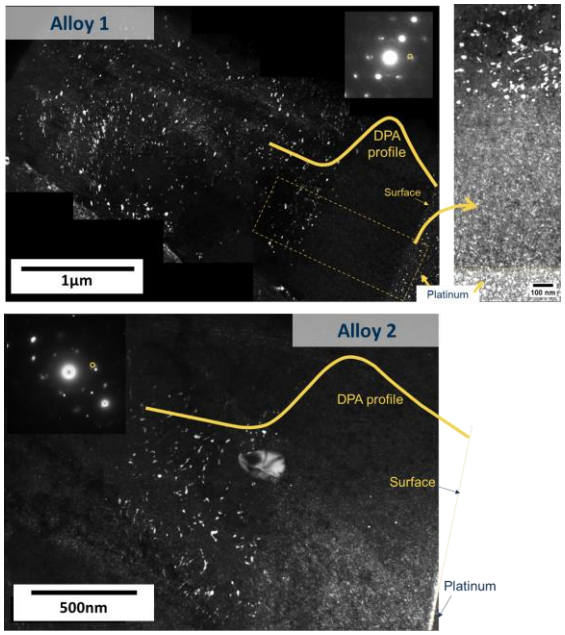

Figure 3: Dark-field TEM micrographs of Alloy 1 and Alloy 2, showing the ion-irradiated layer in which a dramatic decline in MX precipitates can be seen. Shown right of Alloy 1 is the irradiated layer with increased brightness/contrast.

tips to minimise Ga contamination. For the samples taken from the irradiated region, Pt deposition was used to track the incident surface such that the APT needle apexes could be positioned at a known depth into the dpa profile (this was either 500 nm or 600 nm for the samples used in this study). Data was collected via both voltage (20% pulse fraction, 200 kHz pulse frequency) and laser pulsing methods (40 pJ pulse energy, 200 kHz pulse frequency) at a temperature of 50 K. IVAS 3.8.16 and AP Suite IVAS 6.3 were used to reconstruct the raw APT data.

The series of micrographs in Figure 2 shows the typical intragranular precipitates in Alloy 1, in the unirradiated state (micrographs captured from unirradiated regions of the irradiated samples). The reflections associated with the MX phase are very weak and cannot be readily identified in the diffraction patterns. However, the precipitates showed strong contrast in dark-field images produced by aligning the smallest objective aperture with the expected position of reflections associated with an FCC VN phase, with Baker-Nutting orientation relationship to the matrix. In each of the micrographs in Figure 3, the diffraction pattern is shown top left, and position of the objective aperture is shown by a yellow circle. The Baker-Nutting relationship implies that for each micrograph, only a third of the total MX phase is visible, thus a number density of should be taken to be 3x the number visible in a given dark-field micrograph. The precipitates are mostly needle-like in morphology, though some are more plate-like. The number density and sizes of the precipitates are similar in both alloys with a number density of ~$1x10^{22}$ /m^3, mean length ~16 nm, and mean width ~5 nm, with some needles as narrow as 1 nm.

Figure 3 shows dark-field TEM micrographs depicting typical grains from each alloy that span the entire irradiation depth. The nanoprecipitates are clearly visible in the unirradiated portion of the alloys, but none are visible in the irradiated layer. Figure 4 also shows the irradiated layer of Alloy 1 at higher contrast, in which an increase in white-dots can be seen. This is also visible for Alloy 2. Despite a similar appearance, this contrast is not from fine dislocation loops as the image was not captured using a fundamental matrix reflection. Initial inspection of Figure 3 suggests the VN precipitates have undergone dissolution during irradiation, but it remains to be seen whether any refinement of these precipitates has also occurred – other artefacts may be contributing to the white-dot contrast seen Figure 3. No dependency on the depth in the irradiation profile is evident from these micrographs, suggesting the breakdown of the VN precipitates occurred below a dose of 40 dpa (the minimum dose in the irradiation profile prior to the Bragg peak).

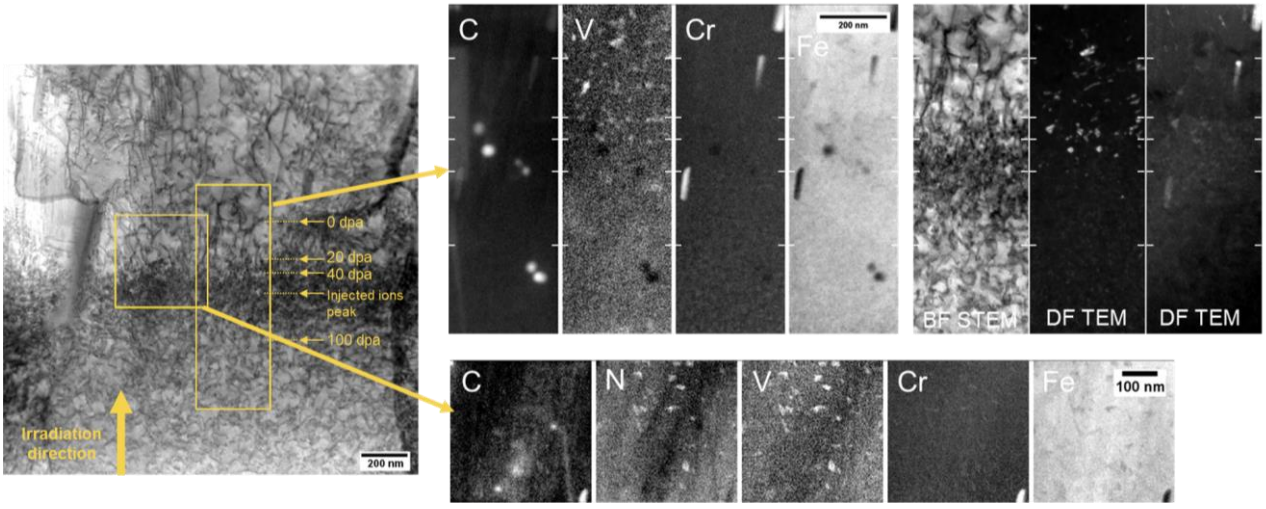

Figure 4: STEM-EELS maps of the microstructure across and close to the Bragg peak. Tick marks are positioned in line with the peak dpa (100 dpa), injected ions peak, and doses 40, 20 and 0 dpa, as labelled for micrograph on the left. Note, the spots in the carbon map are thought to be carbon deposits from when the STEM probe was idle.

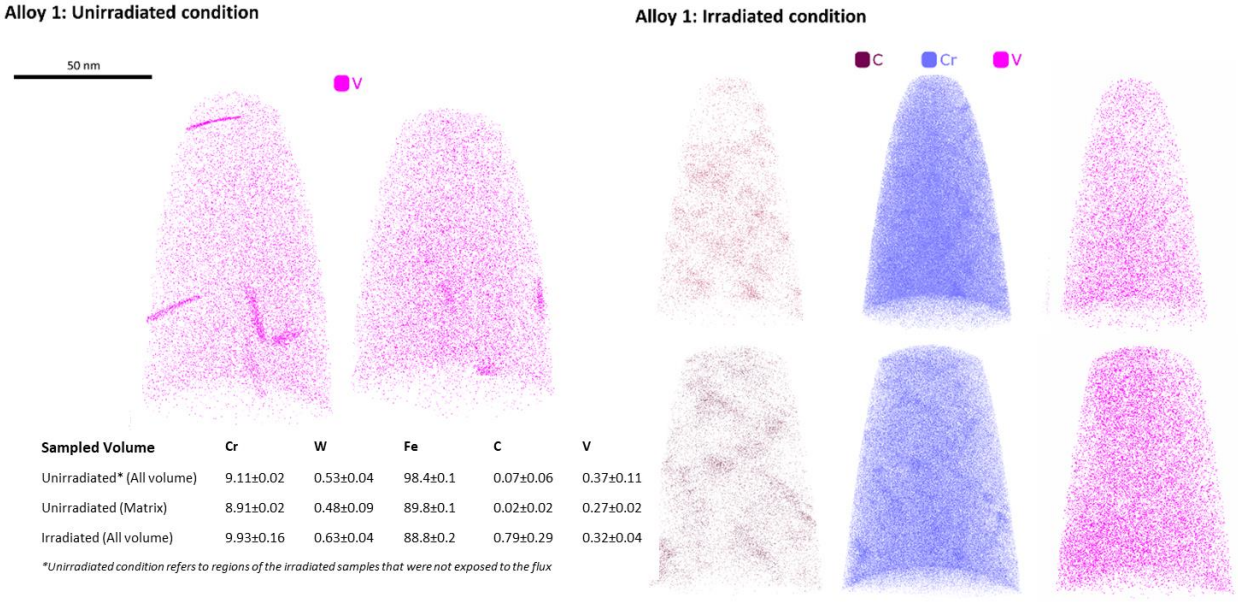

Sampled Volume	Cr	W	Fe	C	V
Unirradiated* (All volume)	9.11±0.02	0.53±0.04	98.4±0.1	0.07±0.06	0.37±0.11
Unirradiated (Matrix)	8.91±0.02	0.48±0.09	89.8±0.1	0.02±0.02	0.27±0.02
Irradiated (All volume)	9.93±0.16	0.63±0.04	88.8±0.2	0.79±0.29	0.32±0.04

**Unirradiated condition refers to regions of the irradiated samples that were not exposed to the flux*

Figure 5: Atom Probe Reconstructions of Alloy 1 in the unirradiated and irradiated conditions. The APT compositions in at% are listed for key elements (± indicates the standard deviation across multiple datasets)

To investigate further the level of dissolution, analytical STEM was carried out on Alloy 1. Figure 4 shows EELS maps of the VN precipitates in Alloy 1, with both the irradiated and unirradiated portions of the microstructure visible. The BF-STEM image in Figure 4 shows a dark horizontal band in the microstructure where the dislocation density is very high, which matches well to the position of the injected interstitials from the ion irradiation. Edges for carbon, nitrogen, carbon, vanadium, chromium and iron were mapped. Also show in Figure 4 are DF-TEM images from the same region. From these, it is clear to see that only after the injected interstitials do we see retention of VN, where dpa is very low.

To ascertain for certain whether any VN is retained in very small clusters, or as small re-precipitated MX phases, APT was used to produce high resolution atomic reconstructions of the unirradiated and irradiated regions of Alloy 1, shown in Figure 5, and of Alloy 2, provided as supplementary data. APT can only sample a small volume per dataset, but was able to capture clear vanadium-rich needle-shaped precipitates, 1-2 nm in diameter, in the unirradiated states of both alloys that match the observations of MX precipitates seen in the TEM. In the irradiated condition, no visual evidence of refined V-rich precipitates could be found, and statistical analysis methods (namely frequency distribution and nearest-neighbour approaches within IVAS software) were applied to the irradiated volumes to clarify is there was any remnant spatial segregation of V – these yielded negative results, indicating that, at least within the volumes analysed, there was no evidence of MX dissolution into smaller clusters/phases. Ultimately, this indicates definitively the complete re-solution of VN precipitates during irradiation. However, APT did reveal co-clustering of carbon and chromium (observable in Figure 5).

Alongside the lack of visible MX precipitates in the atom probe maps, matrix compositions indicate changes to the local compositions with irradiation. There is a significant increase in the C content of needles after irradiation, from 0.07 to 0.79 at%, plus a small increase in matrix V levels as precipitates dissolve, from 0.27 to 0.32 at%. However, these values represent an average value, whereby five datasets had a V content greater than 0.33 at.% and one contained 0.27 at.% - indicative of the sample-to-sample variation at the nanoscale investigated by APT.

The reason for the carbon increase is not clear, but a possible source is from contamination during irradiation. The issue of carbon contamination during ion irradiation is discussed by Wang et al. [22], where carbon concentrations up to ~1 at% were reported for their samples irradiated to 100 dpa under a vacuum of ~7×10^{-5} Pa. For the irradiation reported here, the target chamber vacuum over the course of the irradiation started at ~3×10^{-4} Pa, and dropped steadily to ~5×10^{-5} Pa over the course of the irradiation. The carbon contamination is likely to have adversely affected the fine-scale solute clustering, since chromium clustering is usually suppressed during high dose-rate heavy-ion irradiation in FeCr alloys [23–26], and yet it is quite clearly seen here. Fedorov et al. [27] recently showed how only a small amount of carbon is needed to initiate chromium clustering, and that the chromium content of such clusters is expected to increase as a function of carbon concentration. This could be the source of the white-dot contrast seen in the TEM.

These results demonstrate there is a vulnerability of fine VN precipitates to undergo complete dissolution during irradiation, in contrast to earlier studies on MX precipitates [12–15] which only showed slight or partial dissolution. Dissolution of the VN, through loss of

dispersed barrier strength, may accelerate the recovery of martensite into ferrite and the onset of tertiary creep. The dissolution is likely to have been preceded by fragmentation of the needles, as observed by Tan et al. [14]. No amorphisation of MX was seen; it is unlikely that the MX precipitate dissolution was preceded by a crystalline to amorphous transition as is seen for other precipitates. Amorphisation destabilises the precipitate, and can accelerate the onset of re-solution with the matrix [28,29]. MX phases have much higher melting temperatures than $M_{23}C_6$, and thus higher crystalline-glass transition temperatures may also be expected. Thus, one might expect MX to also be susceptible to amorphisation, and potentially up to higher temperatures than $M_{23}C_6$. However, Bhattacharya et al. [30] found MX to have an inherent resistance to amorphisation. This resistance, and the fragmentation observed by Tan et al. [14], indicates that the dissolution seen here is unlikely to have been preceded by an amorphous phase.

The size of the precipitates could affect their susceptibility to dissolution, since the narrow morphology (1-2nm) of the needles is likely to be less than the size of the collision cascade. By this reasoning, it is reasonable to expect a lower surface-area morphology precipitate (e.g. a spherical precipitate in the ideal case) to have a better resistance to fragmentation and dissolution during irradiation.

The effect of dose-rate could also have exacerbated the dissolution rate. At the high dose rate ~10^{-3} dpa/s used here, the microstructure has little time to recover before a subsequent cascades are encountered. This means any damage to fine precipitates has limited capacity to repair. For context, the studies by Tanigawa et al. [10,11] included both ion-irradiated (up to 20 dpa) and neutron-irradiated (5 dpa) alloys, and in both cases dissolution of the MX phase (TaC) was observed. However, the lower temperatures (300 or 500^{o}C) could mean amorphisation plays a greater role in the dissolution in these studies, so it is not possible to infer from this work how much dose-rate may have affected the dissolution during higher temperature irradiation (600^{o}C) reported here. The works by Tan et al. [12,14] examined alloys irradiated with ions at a dose rate ~10^{-4} dpa/s at 500^{o}C, and observed fragmentation and some dissolution of VN from ~70-130 dpa [14], but little change for doses below 50 dpa [12,14]. Finally, Kano et al. [13] also observed little change to the TaC after ion irradiation to ~50 dpa at a dose rate of ~10^{-3} dpa/s at 400^{o}C. Here, we have reported completed dissolution throughout the damage profile (before the injected interstitial peak), from ~40-100 dpa, and at this same dose-rate as Kano et al. [13]. There does not appear to be a consistent trend from these studies; thus, while high-dose rate ion-irradiation experiments such as these are useful for identifying the potential for dissolution, extensive experiments are required which vary dose-rate, dose and temperature to evaluate the significance of MX instability during reactor conditions in a common alloy. Ideally, more studies on neutron irradiated samples are required. This will all be the subject of further investigations.

In conclusion, this study highlights the susceptibility of fine VN precipitates to undergo complete dissolution during ion irradiation, challenging existing notions derived from studies on MX precipitates. The observed dissolution, likely influenced by the small precipitate size, underscores the need for further investigations focussing on dose, dose-rate, temperature and morphology. Particularly, the MX behaviour under neutron irradiation requires careful investigation in order to identify the severity of dissolution under fusion-like conditions.

Acknowledgement

The authors acknowledge support from the UK EPSRC Fusion Grant 2022/27, EP/W006839/1. This research was also supported by UKAEA and ANSTO, as part of the International Science Partnerships Fund (ISPF). The alloys used in this study were developed with support from the Research Wales Innovation Fund Collaboration Booster 2021, PROJECT #FF2. STEM was performed using the 'South of England Analytical Electron Microscope' at the University of Oxford, supported by EPSRC grant EP/K040375/1. The research used UKAEA's Materials Research Facility, which has been funded by and is part of the UK's National Nuclear User Facility and Henry Royce Institute for Advanced Materials (EP/P021727/1). The atom probe facilities at the University of Oxford are funded by the EPSRC grants EP/M022803/1 and EP/T011505/1.

Declaration of Generative AI and AI-assisted technologies in the writing process

Statement: During the preparation of this work the author(s) used ChatGPT-3.5 in order to check the manuscript and make suggested changes to aid readability. After using this tool/service, the author(s) reviewed and edited the content as needed and take(s) full responsibility for the content of the publication.

References

[1] C. Cabet, F. Dalle, E. Gaganidze, J. Henry, H. Tanigawa, Ferritic-martensitic steels for fission and fusion applications, J. Nucl. Mater. 523 (2019) 510–537. https://doi.org/10.1016/J.JNUCMAT.2019.05.058.

[2] L. Tan, Y. Katoh, L.L. Snead, Development of castable nanostructured alloys as a new generation RAFM steels, J. Nucl. Mater. 511 (2018) 598–604. https://doi.org/10.1016/J.JNUCMAT.2018.05.024.

[3] M. Rieth, E. Simondon, G. Pintsuk, G. Aiello, J. Henry, D. Terentyev, A. Puype, C. Cristalli, L. Pilloni, O. Tassa, M. Klimenkov, H.C. Schneider, P. Fernandez, T. Gräning, X. Chen, A. Bhattacharya, J. Reed, J.W. Geringer, M. Sokolov, Y. Katoh, L. Snead, Technological aspects in blanket design: Effects of micro-alloying and thermo-mechanical treatments of EUROFER97 type steels after neutron irradiation, Fusion Eng. Des. 168 (2021) 112645. https://doi.org/10.1016/J.FUSENGDES.2021.112645.

[4] A. Bhattacharya, S.J. Zinkle, J. Henry, S.M. Levine, P.D. Edmondson, M.R. Gilbert, H. Tanigawa, C.E. Kessel, Irradiation damage concurrent challenges with RAFM and ODS steels for fusion reactor first-wall/blanket: A review, JPhys Energy. 4 (2022) 0–51. https://doi.org/10.1088/2515-7655/ac6f7f.

[5] A. Bhattacharya, X. Chen, T. Graening, J.W. Geringer, J. Reed, J.

Henry, L. Pilloni, D. Terentyev, A. Puype, T.S. Byun, Y. Katoh, M. Rieth, S.J. Zinkle, Irradiation hardening and ductility loss of Eurofer97 steel variants after neutron irradiation to ITER-TBM relevant conditions, Fusion Eng. Des. 173 (2021) 112935. https://doi.org/10.1016/J.FUSENGDES.2021.112935.

[6] F Abe, Creep Resistant Steels, Alpha Science International, 2004.

[7] M. Duerrschnabel, U. Jäntsch, R. Gaisin, M. Rieth, Microstructural insights into EUROFER97 batch 3 steels, Nucl. Mater. Energy. 35 (2023) 101445. https://doi.org/10.1016/J.NME.2023.101445.

[8] R.L. Klueh, P.J. Maziasz, The microstructure of chromium-tungsten steels, Metall. Trans. A. 20 (1989) 373–382. https://doi.org/10.1007/BF02653916/METRICS.

[9] A. Puype, L. Malerba, N. De Wispelaere, R. Petrov, J. Sietsma, Effect of processing on microstructural features and mechanical properties of a reduced activation ferritic/martensitic EUROFER steel grade, J. Nucl. Mater. 494 (2017) 1–9. https://doi.org/10.1016/J.JNUCMAT.2017.07.001.

[10] H. Tanigawa, H. Sakasegawa, R.L. Klueh, Irradiation Effects on Precipitation in Reduced-Activation Ferritic/Martensitic Steels, Mater. Trans. 46 (2005) 469–474. https://doi.org/10.2320/MATERTRANS.46.469.

[11] H. Tanigawa, H. Sakasegawa, H. Ogiwara, H. Kishimoto, A. Kohyama, Radiation induced phase instability of precipitates in reduced-activation ferritic/martensitic steels, J. Nucl. Mater. 367–370 (2007) 132–136. https://doi.org/10.1016/J.JNUCMAT.2007.03.155.

[12] L. Tan, Y. Katoh, L.L. Snead, Stability of the strengthening nanoprecipitates in reduced activation ferritic steels under Fe2+ ion irradiation, J. Nucl. Mater. 445 (2014) 104–110. https://doi.org/10.1016/J.JNUCMAT.2013.11.003.

[13] S. Kano, H. Yang, J. Shen, Z. Zhao, J. McGrady, D. Hamaguchi, M. Ando, H. Tanigawa, H. Abe, Instability of MX and M23C6 type precipitates in F82H steels under 2.8 MeV Fe2+ irradiation at 673 K, Nucl. Mater. Energy. 17 (2018) 56–61. https://doi.org/10.1016/J.NME.2018.08.001.

[14] L. Tan, B.K. Kim, G.S. Was, Evolution dependence of vanadium nitride nanoprecipitates on directionality of ion irradiation, J. Nucl. Mater. 495 (2017) 425–430. https://doi.org/10.1016/J.JNUCMAT.2017.09.001.

[15] L. Tan, W. Zhong, T. Chen, Microstructural stability of tantalum-alloyed ferritic-martensitic steel with neutron irradiation to 7.4 dpa at ~490 °C, Materialia. 9 (2020) 100608. https://doi.org/10.1016/J.MTLA.2020.100608.

[16] J.F. Ziegler, M.D. Ziegler, J.P. Biersack, SRIM - The stopping and range of ions in matter (2010), Nucl. Instruments Methods Phys. Res. Sect. B Beam Interact. with Mater. Atoms. 268 (2010) 1818–1823. https://doi.org/10.1016/j.nimb.2010.02.091.

[17] R.E. Stoller, M.B. Toloczko, G.S. Was, A.G. Certain, S. Dwaraknath, F.A. Garner, Erratum to “On the use of SRIM for computing radiation damage exposure” [Nucl. Instrum. Methods Phys. Res. B 310 (2013) 75–80], Nucl. Instruments Methods Phys. Res. Sect. B Beam Interact. with Mater. Atoms. 459 (2019) 196–197. https://doi.org/10.1016/J.NIMB.2019.08.015.

[18] R.E. Stoller, M.B. Toloczko, G.S. Was, A.G. Certain, S. Dwaraknath, F.A. Garner, On the use of SRIM for computing radiation damage exposure, Nucl. Instruments Methods Phys. Res. Sect. B Beam Interact. with Mater. Atoms. 310 (2013) 75–80. https://doi.org/10.1016/j.nimb.2013.05.008.

[19] L.A. Giannuzzi, J.L. Drown, S.R. Brown, R.B. Irwin, F.A. Stevie, Applications of the FIB lift-out technique for TEM specimen preparation, Microsc. Res. Tech. 41 (1998) 285–290. https://doi.org/10.1002/(SICI)1097-0029(19980515)41:4<285::AID-JEMT1>3.0.CO;2-Q.

[20] M.K. Miller, K.F. Russell, Atom probe specimen preparation with a dual beam SEM/FIB miller, Ultramicroscopy. 107 (2007) 761–766. https://doi.org/10.1016/J.ULTRAMIC.2007.02.023.

[21] CrystalMaker Software: Crystal & Molecular Structures Modelling and Diffraction, (n.d.). http://crystalmaker.com/index.html (accessed September 3, 2018).

[22] J. Wang, M.B. Toloczko, K. Kruska, D.K. Schreiber, D.J. Edwards, Z. Zhu, J. Zhang, Carbon Contamination during Ion Irradiation-Accurate Detection and Characterization of its Effect on Microstructure of Ferritic/Martensitic Steels, Sci. Rep. 7 (2017). https://doi.org/10.1038/S41598-017-15669-Y.

[23] J.C. Haley, S. de Moraes Shubeita, P. Wady, A.J. London, G.R. Odette, S. Lozano-Perez, S.G. Roberts, Microstructural examination of neutron, proton and self-ion irradiation damage in a model Fe9Cr alloy, J. Nucl. Mater. (2020) 152130. https://doi.org/10.1016/j.jnucmat.2020.152130.

[24] Y. Zhao, A. Bhattacharya, C. Pareige, C. Massey, P. Zhu, J.D. Poplawsky, J. Henry, S.J. Zinkle, Effect of heavy ion irradiation dose rate and temperature on α’ precipitation in high purity Fe-18%Cr alloy, Acta Mater. 231 (2022) 117888. https://doi.org/10.1016/J.ACTAMAT.2022.117888.

[25] E.R. Reese, N. Almirall, T. Yamamoto, S. Tumey, G. Robert Odette, E.A. Marquis, Dose rate dependence of Cr precipitation in an ion-irradiated Fe18Cr alloy, Scr. Mater. 146 (2018) 213–217. https://doi.org/10.1016/J.SCRIPTAMAT.2017.11.040.

[26] R.W. Harrison, A.W. Carruthers, J.A. Hinks, M.G. Burke, S.E. Donnelly, Cascade size and dose rate effects on α’ precipitation in ion-irradiated Fe14Cr alloy, Scr. Mater. 172 (2019) 33–37. https://doi.org/10.1016/J.SCRIPTAMAT.2019.06.034.

[27] M. Fedorov, J.S. Wróbel, A.J. London, K.J. Kurzydłowski, C.C. Fu, T. Tadić, S.L. Dudarev, D. Nguyen-Manh, Precipitation of Cr-rich clusters in Fe-Cr alloys: Effects of irradiation from first principles modeling and experimental observations, J. Nucl. Mater. 587 (2023) 154715. https://doi.org/10.1016/J.JNUCMAT.2023.154715.

[28] S. Kano, H. Yang, J. McGrady, D. Hamaguchi, M. Ando, H. Tanigawa, H. Abe, Study of radiation-induced amorphization of M23C6 in RAFM steels under iron irradiations, J. Nucl. Mater. 533 (2020) 152088. https://doi.org/10.1016/J.JNUCMAT.2020.152088.

[29] X.T. Zu, K. Sun, M. Atzmon, L.M. Wang, L.P. You, F.R. Wan, J.T. Busby, G.S. Was, R.B. Adamson, Effect of proton and Ne irradiation on the microstructure of Zircaloy 4, Philos. Mag. 85 (2005) 649–659. https://doi.org/10.1080/14786430412331320017.

[30] A. Bhattacharya, S.M. Levine, S.J. Zinkle, W.Y. Chen, P. Baldo, C.M. Parish, P.D. Edmondson, Radiation induced amorphization of carbides in additively manufactured and conventional ferritic-martensitic steels: In-situ experiments on extraction replicas, J. Nucl. Mater. 563 (2022) 153646. https://doi.org/10.1016/J.JNUCMAT.2022.153646.

Supplementary material to “Complete dissolution of MX-phase nanoprecipitates in fusion steels during irradiation by heavy-ions”

Jack Haley[ac], Stephen Jones[b], Shahin Mehraban[b], Nicholas Lavery[b], Jonathan Cullen[b], Megan Carter[c], Michael Moody[c], Huw Dawson[ad], David Bowden[a]

[a] *UKAEA, Culham Campus, Abingdon, Oxfordshire OX14 3DB, UK*

[b] *Future Manufacturing Research Institute, College of Engineering, Swansea University, Bay Campus, Fabian Way, Swansea, SA1 8EN, UK*

[c] *Department of Materials, University of Oxford, Parks Road, Oxford OX1 3PH, UK*

[d] *Frazer-Nash Consultancy Limited, Hill Park Court, Springfield Drive, Leatherhead, Surrey, KT22 7NL*

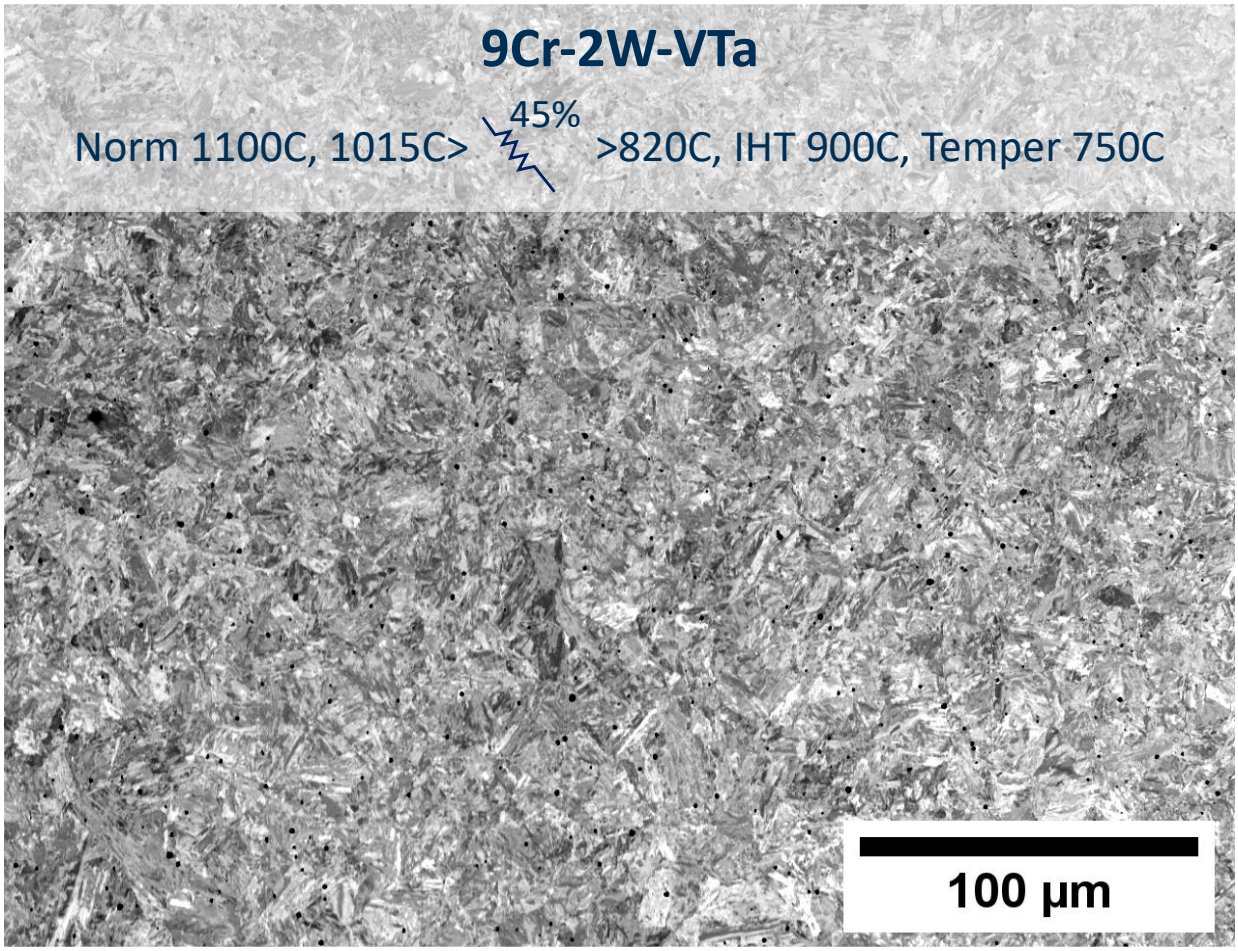

Supplementary Figure S1: SEM Backscatter micrograph of Alloy 1. The thermomechanical heat treatments applied to this steel are noted, top.

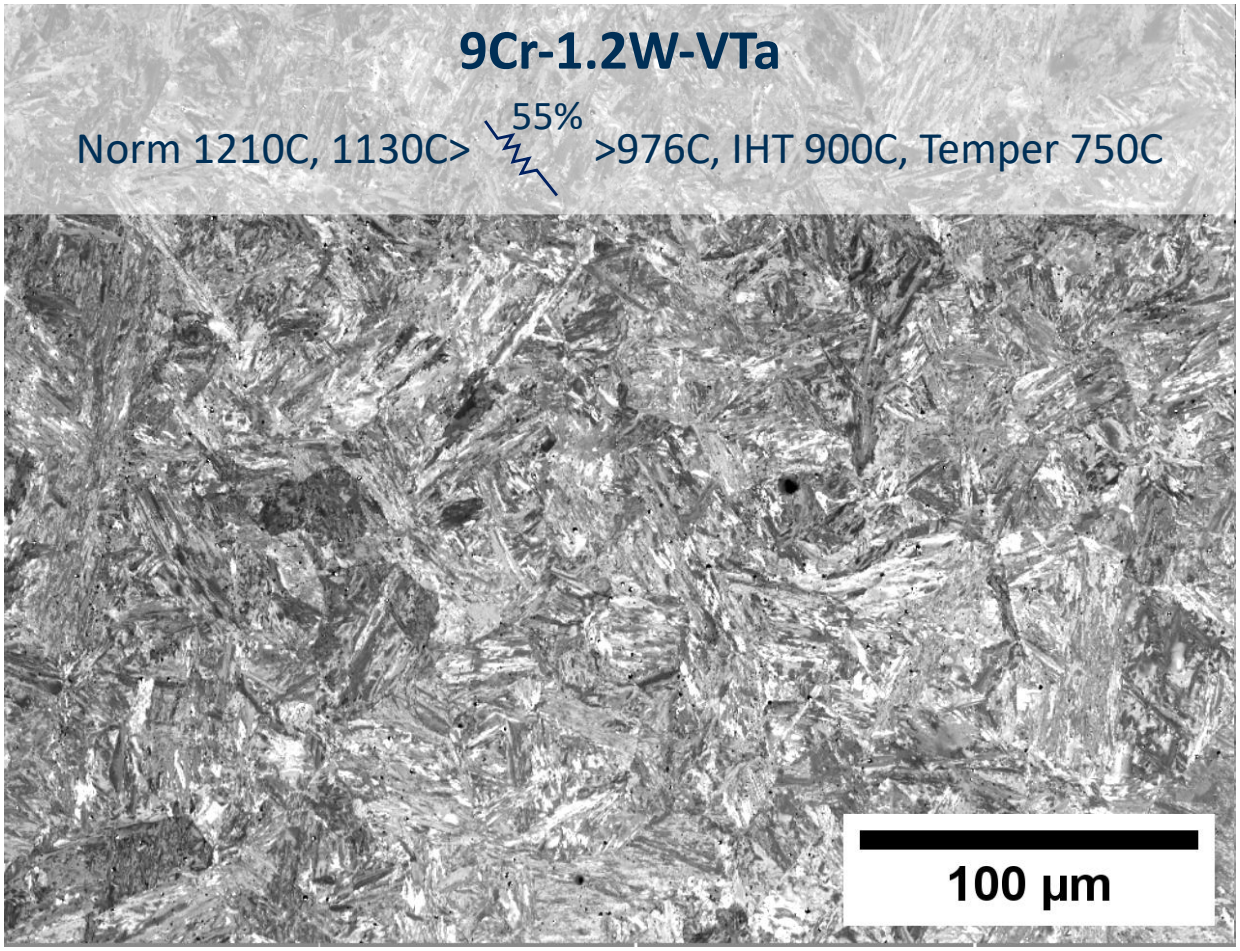

Supplementary Figure S2: SEM Backscatter micrograph of Alloy 1. The thermomechanical heat treatments applied to this steel are noted, top.

Supplementary Figure S3: Alloy 1 APT datasets

Needle #163014 – Irradiated

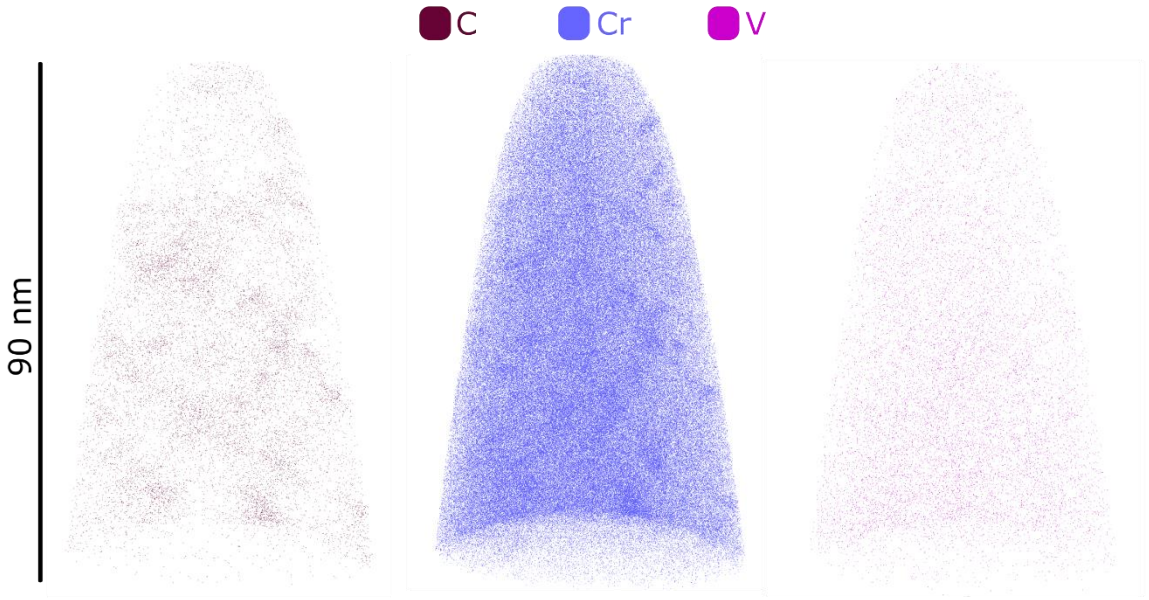

Needle #163015 - Irradiated

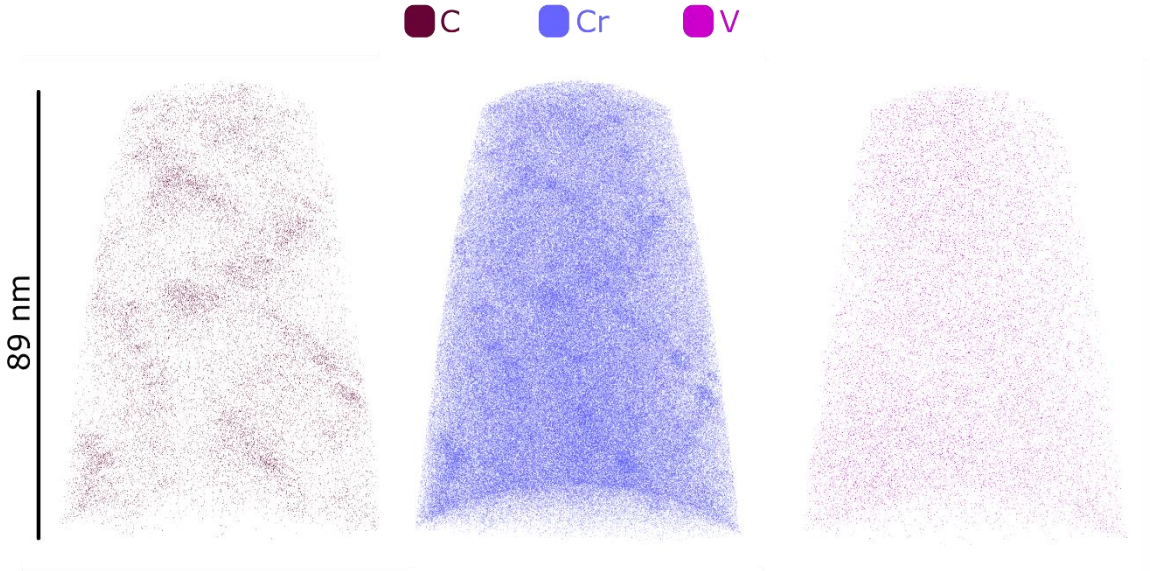

Needle #183169 - Irradiated

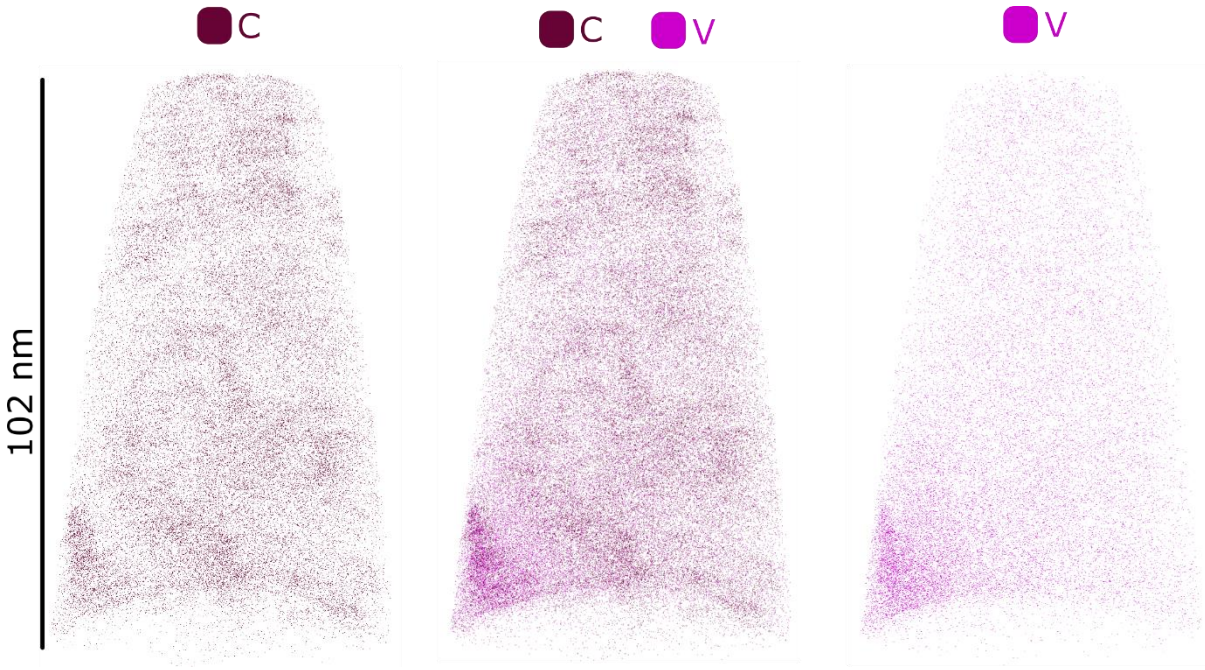

Needle #173108 – Unirradiated

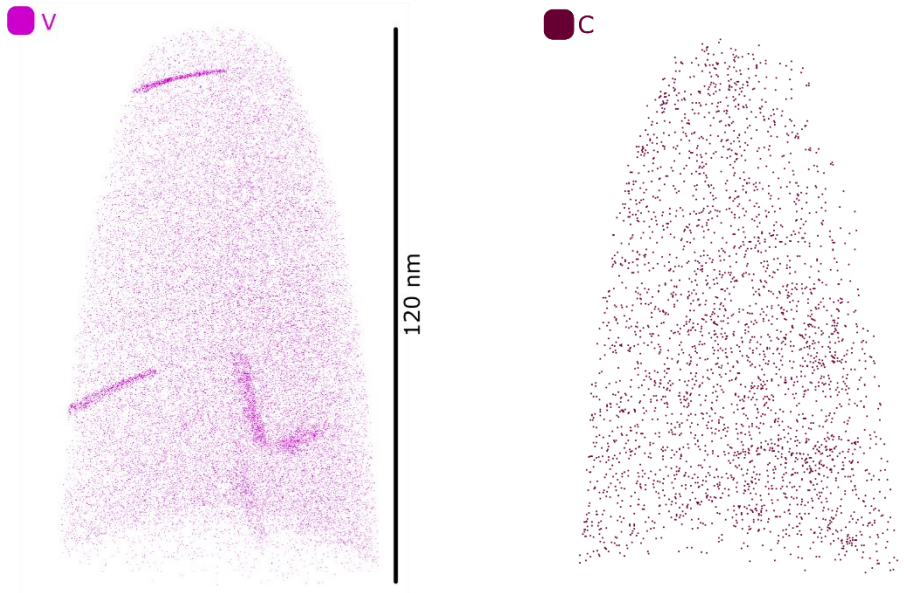

Needle #173110 – Unirradiated

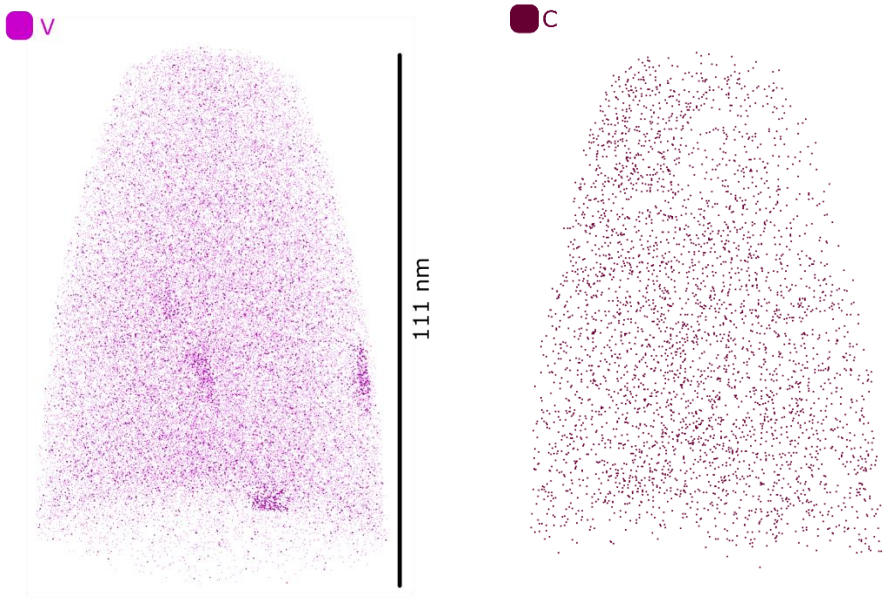

Supplementary Figure S4: Alloy 2 APT datasets

Needle #203483- Irradiated – VN precipitates seen at a depth beyond the expected Bragg peak of the irradiation damage (samples taken from approx. 500 nm depth from surface)

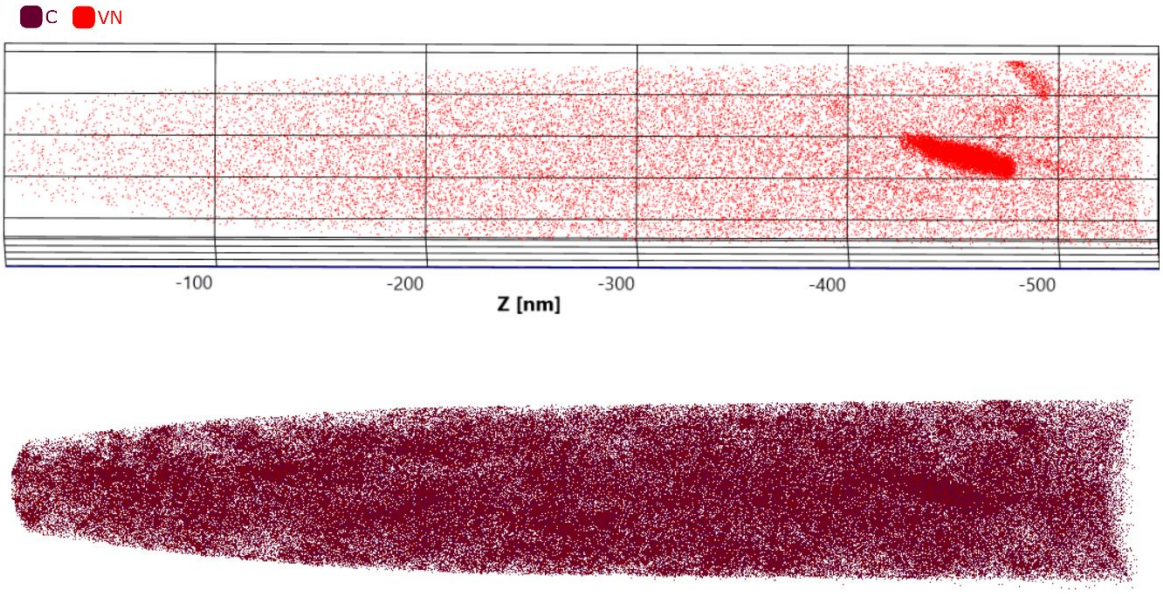

Needle #203530 – Irradiated

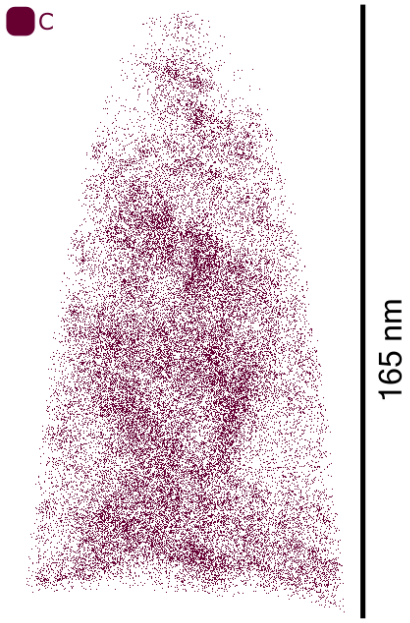

Needle #203739 – Unirradiated

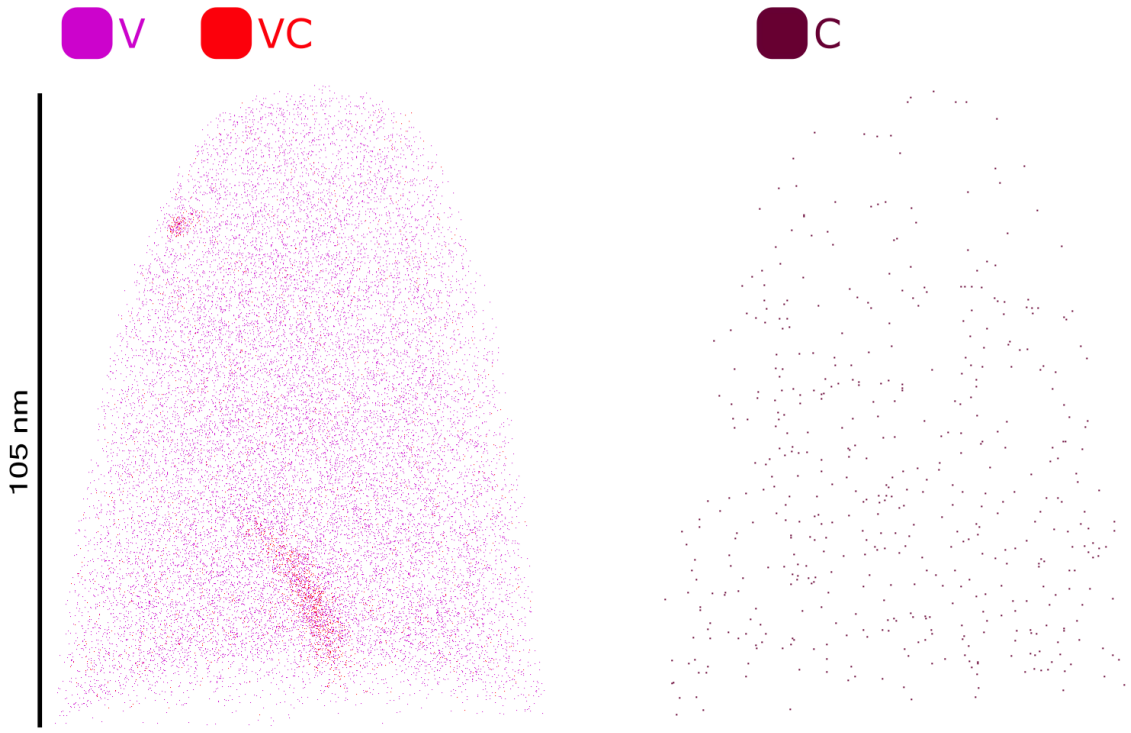

Needle #203742 – Unirradiated

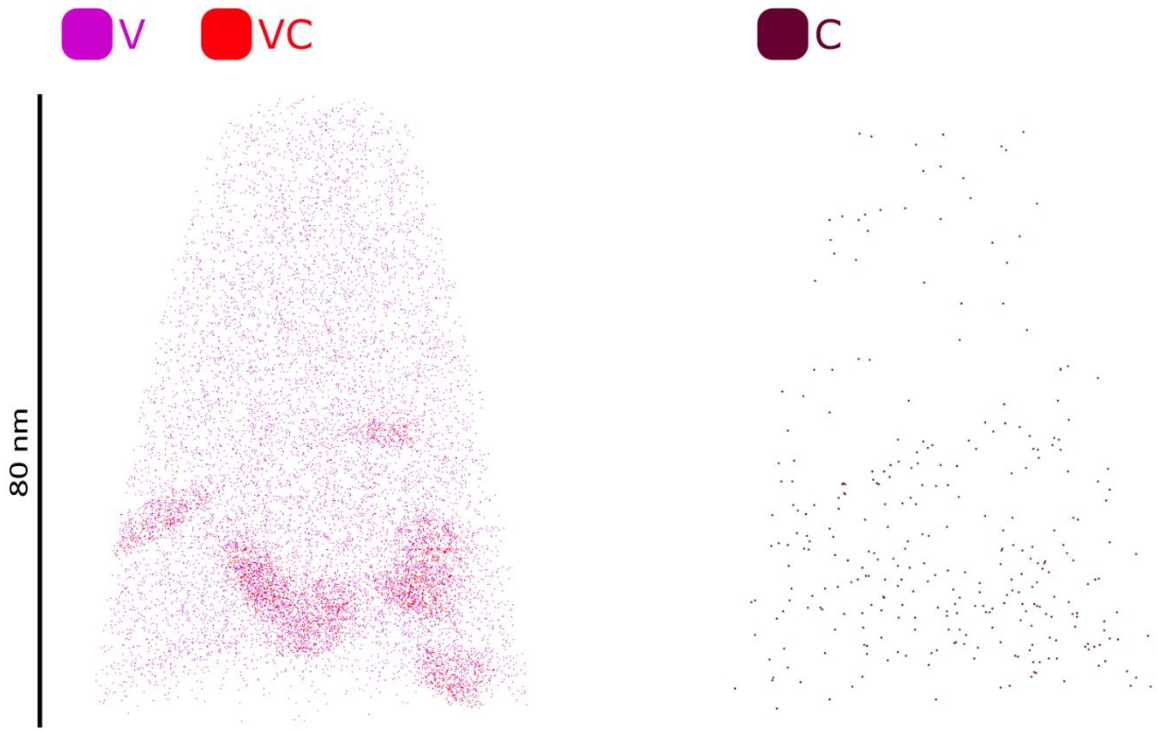
V
VC
C
80 nm